

Interacting bumps model of item limits in working memory

Nikhil Krishnan · Daniel B. Poll · Zachary P. Kilpatrick

Received: date / Accepted: date

Abstract Working memory (WM) is limited in its temporal length and capacity. Classic conceptions of WM capacity assume the system possesses a finite number of slots, but recent evidence suggests WM may be a continuous resource. Resource models typically assume there is no hard upper bound on the number of items that can be stored, but WM fidelity decreases with the number of items. We analyze a neural field model of multi-item WM that associates each item with the location of a bump in a finite spatial domain, considering items that span a one-dimensional continuous feature space. Our analysis relates the neural architecture of the network to accumulated errors and capacity limitations arising during the delay period of a multi-item WM task. Networks with stronger synapses support wider bumps that interact more, whereas networks with weaker synapses support narrower bumps that are more susceptible to noise perturbations. There is an optimal synaptic strength that both limits bump interaction events and the effects of noise perturbations. This optimum shifts to weaker synapses as the number of items stored in the network is increased. Our model not only provides a neural circuit explanation for WM capacity, but also speaks to how capacity relates to the arrangement of stored items in a feature space.

Keywords bump attractor, working memory, capacity, limited resource, interface methods

1 Introduction

Working memory (WM) is defined by both its short timescale and its capacity limitations (Ma et al, 2014). Detailed behavioral and electrophysiological recordings have demonstrated the WM is associated with persistent neural activity in a number of cortical regions (Constantinidis and Klingberg, 2016). Neural and synaptic activity fluctuations account for commonly observed errors accumulated during the delay-period of typical WM tasks (Compte et al, 2000; Wimmer et al, 2014). However, there is controversy surrounding the origin of errors arising from limitations of WM capacity. Classic models contend that item-limits are best defined by a ‘slot model,’ placing a hard upper bound on the number of items that can be stored (Cowan, 2010; Luck and Vogel, 1997). On the other hand, recent work suggests a ‘resource model,’ showing there may be no item-number limit, and better defined by a continuous resource that can be spread across any number of items a subject must remember (Bays and Husain, 2008; Van den Berg et al, 2012; Keshvari et al, 2013; Wilken and Ma, 2004).

N. Krishnan
Department of Applied Mathematics, University of Colorado Boulder
Boulder CO 80309 USA
E-mail: Nikhil.Krishnan@colorado.edu

D.B. Poll
Department of Engineering Sciences and Applied Mathematics, Northwestern University
Evanston IL 60208 USA
E-mail: daniel.poll@northwestern.edu

Z.P. Kilpatrick
Department of Applied Mathematics, University of Colorado Boulder
Boulder CO 80309 USA
E-mail: zpkilpat@colorado.edu

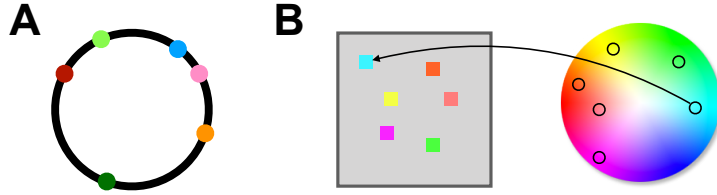


Fig. 1 Examples of multi-item visual stimuli used in working memory tasks (Bays et al, 2009; Ma et al, 2014; Zhang and Luck, 2008). **A.** Memoranda here are angles on a circle corresponding to the dot locations, identified by their color. Subject will be required to store all objects in their memory and then just recall one item; e.g., the location of the blue dot. **B.** Subjects alternatively may have to store and remember the color of each item. For example, a subject may be asked what the color of the top left square was.

Both the slots model and the resource model reproduce some gross statistics from WM tasks. For example, the recall variability tends to increase in both models for a WM task with a high number of items (Bays et al, 2009; Luck and Vogel, 2013). However, for lower numbers of items, response variability is flat in a slots model whereas it increases in a resource model. In addition, more task-relevant cues can be stored with higher precision in a continuous resource model, but not in a slots model. Recent experiments have demonstrated that WM precision varies for low item counts (Bays et al, 2009) and for cued versus uncued items (Gorgoraptis et al, 2011). These results have been recapitulated in several human and non-human primate studies, suggesting flexibility in the allocation of WM (Buschman et al, 2011; Lara and Wallis, 2012). Resource models of WM allow for such flexibility, suggesting many possibilities for how storage precision varies across task parameters (Van den Berg et al, 2012; Fougny et al, 2012).

Computational models that capture behavioral patterns in multi-item WM are an active area of research (Barak and Tsodyks, 2014). It remains an open question what neural mechanisms underlie these trends in response variability. Recent studies have extended the framework of continuous attractor networks, successful in capturing error accumulation in single-item WM tasks (Wimmer et al, 2014), to account for errors observed in multi-item WM (Almeida et al, 2015; Wei et al, 2012). These models are well-suited to store memoranda drawn from a continuous space, such as an angle on a circle (See Fig. 1). Recurrent networks comprised of a locally excitatory population, coupled to a broadly tuned inhibitory population, produce “bumps” of persistent neural activity (Amari, 1977; Compte et al, 2000). Bumps encode the remembered location of a presented angle during the WM delay period, and fluctuations arising from stochastic firing or synaptic transmission degrade memory of the initial position (Compte et al, 2000; Kilpatrick et al, 2013). Multi-item WM errors arise in these models via the interactions of multiple bumps, each encoding a distinct angle (Almeida et al, 2015; Wei et al, 2012). Bumps can repel each other or merge, depending on their proximity, through the nonlocal synaptic interactions of the network. For randomly chosen angles, the relative precision of recall decreases with set size according to a power law (Wei et al, 2012), as in Bays and Husain (2008). Thus, a multiple bumps model of WM appears to reconcile observed behavioral trends with known neural circuit mechanisms for storing WM using persistent activity.

These previous studies were performed using large-scale spiking simulations, however, and could not draw clear connections between parameters and the output model performance. An advantage of using neural field equations to describe large-scale network interactions is that they are analytically tractable, and their dynamics can often be approximated by low-dimensional systems that solely describe variables of interest (Bressloff, 2012). For instance, previous neural field studies of bump attractor models of single-item WM have developed explicit expressions for the relationship between network connectivity and the response variability (Carroll et al, 2014; Kilpatrick, 2013, 2017). Other work has explored the interaction of multiple bumps in neural field equations, but in a number of special cases that admit a thorough analysis, which are not relevant to the problem of storing an arbitrary set of memoranda (Bressloff, 2005; Laing and Troy, 2003a; Laing et al, 2002; Lu et al, 2011). A robust model for storing multiple angles would allow for multiple bumps to be stored at arbitrary locations around a network. Our study explores tradeoffs in the strength of neural architecture as it impacts bumps’ response to fluctuations, as well as interactions between neighboring bumps.

We utilize interface methods, originally applied to single bump solutions (Amari, 1977; Coombes et al, 2012), to project the dynamics of multiple bumps in a neural field to a low-dimensional system of differential equations for the edges of the bumps. This approximate system can be analyzed in order to uncover the relationship between the architecture of the network and the robustness of multi-item WM. In particular, we examine how bumps interact with one another, and how they respond to external fluctuations applied

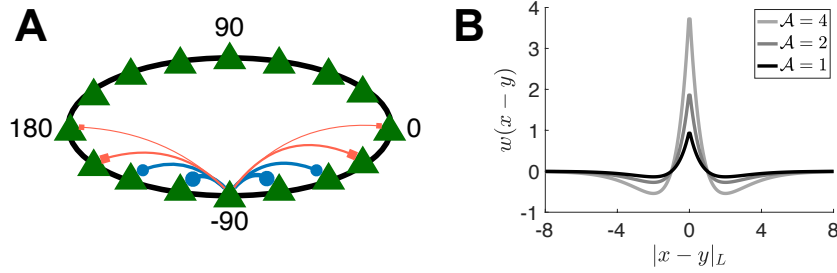


Fig. 2 Recurrent network model of multiple-item WM. **A.** The neural field, Eq. (2.1) is comprised of local populations (green triangles) organized on a ring with distance-dependent connectivity. This single layer describes the activity $u(x, t)$ of a combined excitatory/inhibitory neural field, derived in the limit of fast inhibition (Amari, 1977; Carroll et al, 2014; Pinto and Ermentrout, 2001). Strong effective excitation (blue dots) is short range whereas weaker effective inhibition (red squares) is long range. **B.** Weight function, Eq. (2.2), scaled by different maximal synaptic strengths $\mathcal{A} = \max_{x \in [-L, L]} w(x)$.

to model the known stochastic evolution of persistent activity during the WM delay-period (Wimmer et al, 2014). Interestingly, increasing the strength of synaptic coupling makes networks with bumps that are robust to noise, but each individual bump covers more of the network and is likely to merge with its neighbor. Thus, networks with the lowest response variability have an intermediate value of synaptic strength, which trades off the robustness of large bumps to noise with the increased precision of networks containing smaller bumps.

2 Neural field model of visuospatial working memory

Most bump attractor models of working memory (WM) focus on tasks where a subject must remember a single orientation each trial (Kilpatrick and Ermentrout, 2013; Wimmer et al, 2014). However, WM capacity can be probed by testing subjects' ability to recall multiple items (Bays and Husain, 2008; Zhang and Luck, 2008). We analyze a recurrent, spatially-organized network, which can represent multiple orientations during the delay period of a visuospatial WM task (Almeida et al, 2015). The model is similar to the case of single-item WM, but the network architecture plays an important role in shaping memory capacity (Bays, 2015).

2.1 Model definition

We study a neural field model where locations of neurons correspond to their preferred stimulus orientation, organized in a ring architecture with slow local excitation and broad inhibition (Ermentrout, 1998):

$$du(x, t) = \left[-u(x, t) + \int_{-L}^L w(x-y) H(u(y, t) - \theta) dy \right] dt + \sqrt{\epsilon \cdot |u(x, t)|} dZ(x, t). \quad (2.1)$$

The variable $u(x, t)$ represents synaptic input to spatial location $x \in [-L, L]$ at time t , which is periodic so $u(L, t) = u(-L, t)$. The weight function $w(x-y)$ represents the synaptic connectivity from neurons at location y to location x . Note, we assume the weight function is even $w(x) = w(-x)$, which satisfies periodicity $w(-L) = w(L)$.

We consider the weight function,

$$w(x-y) = \mathcal{A}(1 - |x-y|_L) e^{-|x-y|_L}, \quad (2.2)$$

with local excitation and broad inhibition (Coombes and Owen, 2005), where \mathcal{A} parameterizes the synaptic strength, and $|x|_L = \min(|x-y|, |2L-|x-y||)$ is the distance on the ring (Fig. 2). Note, neurons with similar orientation will tend to activate one another, while neurons with dissimilar orientation tend to inhibit one another. Integrating $\int_{-L}^L w(x-y) dy = 2\mathcal{A}(1 - e^{-L}) - 2\mathcal{A}(1 - (1+L)e^{-L}) = 2\mathcal{A}Le^{-L}$, we find the sum of excitation and inhibition is approximately balanced ($\int_{-L}^L w(x-y) dy \approx 0$) for $L \gg 1$. Since we are interested in focusing on how scaling \mathcal{A} impacts WM capacity for angles, we will fix $L := 180$ consistent with typical oculomotor delayed-response tasks (Constantinidis and Klingberg, 2016; Funahashi et al, 1989; Goldman-Rakic, 1995; Wimmer et al, 2014). The weight function Eq. (2.2) is one example in a class of synaptic

kernels that arises in the limit of fast inhibition such that separate excitatory and inhibitory populations can be combined into a single population Eq. (2.1) (Carroll et al, 2014).

The nonlinearity in Eq. (2.1) is a Heaviside step function

$$H(u - \theta) = \begin{cases} 1, & u > \theta, \\ 0, & u < \theta, \end{cases} \quad (2.3)$$

representing the input-output relationship between post-synaptic activation and the population firing rate at x . A smooth sigmoidal function can also be used, but the qualitative dynamics of Eq. (2.1) remain the same for steep sigmoids (Bressloff, 2012; Coombes and Schmidt, 2010). We exploit the fact that the output of $H(u - \theta)$ is binary ($\{0, 1\}$) to develop interface equations for the dynamics of bumps in Eq. (2.1), adapting methods originally developed by Amari (1977) and extended by Coombes et al (2012).

Rather than modeling the instantiation of bumps in Eq. (2.1) using a spatiotemporal input as in Almeida et al (2015); Compte et al (2000); Kilpatrick et al (2013), we consider bump initiation implemented with initial conditions. Initiating bumps with external input does not significantly alter our results. Stochasticity is modeled by weak and multiplicative noise $\sqrt{\epsilon}u(x, t)dZ(x, t)$, driven by the increment of a spatially-dependent Wiener process such that $\langle dZ(x, t) \rangle = 0$ and $\langle dZ(x, t)dZ(y, s) \rangle = C(x - y)\delta(t - s)dt ds$. The spatial correlations $C(x - y)$ are a symmetric function that depends on the distance between two locations in the network. Typical formulations of Langevin equations take the multiplicative noise to be of Stratonovich form (Gardiner, 2009), and a related neural field equation can be derived by applying a Kramers-Moyal expansion to a neural master equation (Bressloff, 2009).

The impact of multiplicative noise on bump dynamics is analyzed by adapting methods developed for bumps in neural fields with additive noise (Kilpatrick and Ermentrout, 2013). Note, we could modify Eq. (2.1) to account for the systematic shift induced by multiplicative noise in the Stratonovich sense. However, this contribution will be $\mathcal{O}(\epsilon)$ in comparison to the $\mathcal{O}(\sqrt{\epsilon})$ amplitude of the noise itself. Thus, we simply truncate the equation to ignore these additional terms, which would only slightly shift the resulting form of the stationary solution we will linearize about, as discussed in Bressloff and Webber (2012). To be explicit, we note that we can compute $\sqrt{\epsilon}\langle u(x, t)dZ(x, t) \rangle = \epsilon C(0)\langle \text{sign}[u(x, t)] \rangle dt/2$ (Novikov, 1965), smaller than the $\sqrt{\epsilon}$ -amplitude noise term we consider. Note, we have run simulations of both the original Eq. (2.1) and the associated mean-corrected equations, and the results are not noticeably different.

2.2 Single bump solutions

Solutions to Eq. (2.1) can be found explicitly when considering specific weight functions (Bressloff, 2012). In particular, stable single bump (stationary pulse) solutions exist when $w(x)$ satisfies requirements making it laterally inhibitory (Amari, 1977), as Eq. (2.2) is. We construct this solution and demonstrate the use of the interface method for characterizing non-equilibrium dynamics of perturbed bump solutions. This will guide our understanding for applying the interface method to multi-bump solutions.

In the absence of stochasticity ($Z \equiv 0$), stationary solutions to Eq. (2.1) satisfy $u(x, t) \equiv U(x)$, leading to the implicit equation

$$U(x) = \int_{-L}^L w(x - y)H(U(y) - \theta)dy. \quad (2.4)$$

Unimodal stationary bumps possess a simply-connected active region $\bar{A} = [\bar{x}_1, \bar{x}_2] = \{x | U(x) \geq \theta\}$ (assuming $-L \leq \bar{x}_1 < \bar{x}_2 < L$), which allows us to rewrite Eq. (2.4) as

$$U(x) = \int_{\bar{x}_1}^{\bar{x}_2} w(x - y)dy. \quad (2.5)$$

For analytical convenience, the translation symmetry of the network Eq. (2.1) is utilized to shift solutions so they are centered at zero (Bressloff, 2012; Ermentrout, 1998):

$$U_0(x) = \int_{-h}^h w(x - y)dy, \quad (2.6)$$

where $h = (\bar{x}_2 - \bar{x}_1)/2$. We show this by using Eq. (2.5) writing the equation for

$$U(x - (\bar{x}_1 + \bar{x}_2)/2) = \int_{-(\bar{x}_2 - \bar{x}_1)/2}^{(\bar{x}_2 - \bar{x}_1)/2} w(x - z)dz = U_0(x),$$

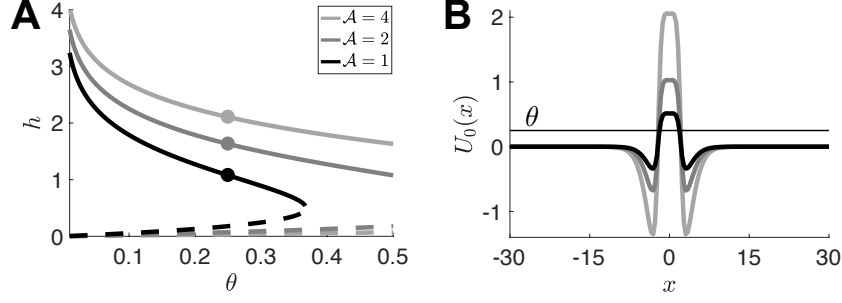


Fig. 3 A. Width of bumps, stable (solid) and unstable (dashed), computed using the threshold condition, Eq. (2.10). Stable bump width increases with the synaptic strength \mathcal{A} . **B.** Examples of bump profiles corresponding to the dots in **A**, widening as \mathcal{A} is increased for fixed $\theta = 0.25$.

where we made the substitution $z = y + (\bar{x}_1 + \bar{x}_2)/2$.

Linear stability of stationary bumps can be determined by examining the evolution of perturbations $u(x, t) = U_0(x) + \varepsilon\psi(x, t) + \mathcal{O}(\varepsilon^2)$ to the bump profile. Linearizing Eq. (2.1) leads to the following evolution equation for the perturbation

$$\psi_t(x, t) = -\psi(x, t) + \int_{-L}^L w(x - y)H'(u(y, t) - \theta)\psi(y, t)dy. \quad (2.7)$$

Separability of solutions $\psi(x, t) = e^{\lambda t}\bar{\psi}(x)$ can be shown (Carroll et al, 2014), yielding the integral equation for linear stability

$$(\lambda + 1)\bar{\psi}(x) = \int_{-L}^L w(x - y)H'(u(y, t) - \theta)\bar{\psi}(y)dy.$$

Note, $(\lambda, \bar{\psi}(x)) = (0, U'_0(x))$ is a solution, since by plugging in we find

$$U'_0(x) = \int_{-L}^L w(x - y)H'(u(y, t) - \theta)U'_0(y)dy, \quad (2.8)$$

and Eq. (2.8) arises by differentiating the stationary bump Eq. (2.4). This indicates the bump is marginally stable to perturbations that shift its position (Amari, 1977; Kilpatrick and Ermentrout, 2013), the main source of error when considering noise and interactions with other bumps.

We perform the integral in Eq. (2.6) for the case of a weight function of form Eq. (2.2). For analytical convenience, we can approximate $L \rightarrow \infty$, obtaining the solution (Coombes and Owen, 2005):

$$U_0(x) = \mathcal{A} \left[(x + h)e^{-|x+h|} - (x - h)e^{-|x-h|} \right]. \quad (2.9)$$

Self-consistency requires the threshold conditions $U(\pm h) = \theta$, yielding an implicit equation for the bump half-width

$$G(h) := U_0(\pm h) = \int_0^{2h} w(y)dy = 2\mathcal{A}he^{-2h} = \theta, \quad (2.10)$$

and we show $h(\theta)$ for different values of synaptic strength \mathcal{A} in Fig. 3A. We also plot stable bump solutions in Fig. 3B, showing they expand in width as the synaptic strength \mathcal{A} is increased.

There are both wide stable and narrow unstable bumps of form Eq. (2.9). A critical value of θ defines the point where these branches of Eq. (2.10) annihilate in a saddle-node (SN) bifurcation (Kilpatrick, 2016). Differentiating with respect to h , the SN bifurcation occurs where $G'(h) = (1 - 2h)2\mathcal{A}e^{-2h} = 0$ which can be solved for $h_c = 1/2$. Plugging $h_c = 1/2$ into Eq. (2.10), we find $\theta_c = \mathcal{A}e^{-1}$. Thus, we select $\theta < \theta_c$ given synaptic strength \mathcal{A} to ensure solution existence. Furthermore, we can differentiate Eq. (2.10) with respect to the synaptic strength \mathcal{A} to yield an expression for

$$\frac{dh}{d\mathcal{A}} = \frac{h}{\mathcal{A}(2h - 1)} > 0,$$

for $h > 1/2$, which occurs for stable bumps as long as $\theta < \theta_c$. Thus, the width of bumps will always increase as \mathcal{A} is increased. Before exploring interactions of multiple bumps of the form of Eq. (2.9), we discuss the interface method we will use to obtain low-dimensional approximations for bump dynamics.

2.3 Interface equations for a single bump

Motivated by solutions of the stationary bump type, as in Eq. (2.5), Amari (1977) developed an interface theory for excitation patterns in the noiseless ($Z \equiv 0$) version of the neural field Eq. (2.1). This approach was recently reviewed in Amari (2014), and has been extended to capture the dynamics of other solutions by Coombes and Laing (2011); Coombes et al (2012). We extend these techniques further to account for stochastic perturbations due to the noise term in Eq. (2.1). Interface equations are derived by noting that the output of the Heaviside nonlinearity, Eq. (2.3), is determined by the active region $A(t) = \{x | u(x, t) \geq \theta\}$ of the spatial domain $x \in [-L, L]$. For a single bump, we define the active region $A(t) = [x_1(t), x_2(t)]$, where the interfaces occur at the boundary points $x_1(t)$ and $x_2(t)$,

$$u(x_j(t), t) = \theta, \quad j = 1, 2. \quad (2.11)$$

We rewrite Eq. (2.1), using our assumed form of the active region $A(t)$ as

$$du(x, t) = \left[-u(x, t) + \int_{x_1(t)}^{x_2(t)} w(x - y) dy \right] dt + \sqrt{\epsilon \cdot |u(x, t)|} dZ(x, t). \quad (2.12)$$

We now derive a stochastic evolution equation for the interfaces, $dx_j = d_j(x_1, x_2, t)dt + g_j(x_1, x_2, t)dz_j$, where d_j is a drift and g_j corresponds to the diffusion term. Differentiating Eq. (2.11) with respect to time, we obtain the following consistency equation for the location of the interfaces $x_j(t)$ and the evolution of the activity variable

$$\alpha_j(t)dx_j(t) + \beta_j(t)(dx_j(t))^2 + du(x_j(t), t) = 0, \quad j = 1, 2, \quad (2.13)$$

where we have defined the spatial gradient at the interface points

$$\alpha_j(t) = \frac{\partial u(x_j(t), t)}{\partial x}, \quad j = 1, 2,$$

and the second derivative $\beta_j(t) = \frac{1}{2}u_{xx}(x_j(t), t)$ for $j = 1, 2$. The middle term in Eq. (2.13) arises from an application of Itô's lemma (Gardiner, 2009). For simplicity, we approximate the spatial gradients using that of the stationary solution for now, $\alpha_1(t) \approx \bar{\alpha} = U'_0(-h)$ and $\alpha_2(t) \approx -\bar{\alpha} = U'_0(h) = -U'_0(-h)$, computed directly from Eq. (2.9). In Coombes et al (2012); Gökçe et al (2017), the dynamic evolution of the gradients $\alpha_j(t)$ is tracked in the case of a deterministic system ($Z \equiv 0$ in Eq. (2.1)). As, discussed, we drop $o(\epsilon)$ terms resulting from multiplicative noise, for simplicity. Thus, the middle term in Eq. (2.13) will vanish, since the noise will have amplitude $\mathcal{O}(\sqrt{\epsilon})$, as we show, and the other terms in $(dx_j)^2$ are vanishingly small. Using the evolution equation for the neural activity, Eq. (2.12), and the interface condition Eq. (2.11), we can describe the evolution of the interfaces by rearranging Eq. (2.13) to find

$$dx_j(t) = \frac{(-1)^j}{\bar{\alpha}} \left(\left[-\theta + \int_{x_1(t)}^{x_2(t)} w(x_j(t) - y) dy \right] dt + \sqrt{\epsilon \cdot \theta} dZ(x_j(t), t) \right), \quad j = 1, 2. \quad (2.14)$$

Since the integral in Eq. (2.14) can be evaluated, we define

$$W(x) = \int_0^x w(y) dy, \quad (2.15)$$

to denote the functions resulting from integration. We can then write

$$\int_{x_1(t)}^{x_2(t)} w(x_j(t) - y) dy = W(x_2(t) - x_1(t)),$$

yielding an even simpler form for the interface equations

$$dx_j(t) = \frac{(-1)^j}{\bar{\alpha}} \left([-\theta + W(x_2(t) - x_1(t))] dt + \sqrt{\epsilon \cdot \theta} dZ(x_j(t), t) \right), \quad j = 1, 2. \quad (2.16)$$

We now remark on a number of observations to be made concerning Eq. (2.16). First, in the absence of noise ($Z \equiv 0$), there is a line of fixed points to the resulting equation

$$\frac{dx_j}{dt} = \frac{(-1)^j}{\bar{\alpha}} (-\theta + W(x_2(t) - x_1(t))), \quad j = 1, 2, \quad (2.17)$$

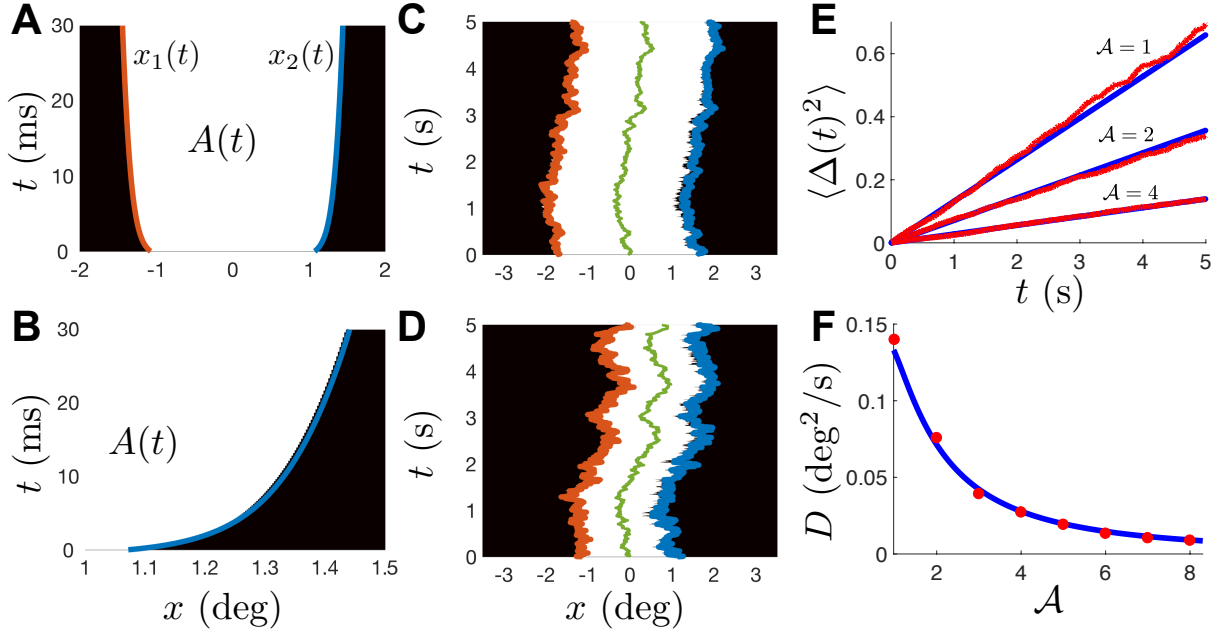


Fig. 4 Low-dimensional interface equations, Eq. (2.16), approximate the dynamics of Eq. (2.1) well for single-bump solutions. **A.** Bump of the form $u(x, 0) = 0.25 \cdot U_0(x)$, Eq. (2.9), expands outward to the equilibrium shape $u(x, t) \rightarrow U_0(x)$ for $\mathcal{A} = 2$. Interface dynamics $u(x_{1,2}(t), t) = \theta$ are well approximated by Eq. (2.18). **B.** Zoom-in of **A.** **C.** Bump initially of form $u(x, 0) = U_0(x)$, for $\mathcal{A} = 2$, evolves stochastically in response to noise with correlation structure Eq. (2.22) with $\epsilon = 0.03$. Interface dynamics approximated by Eq. (2.19). **D.** For $\mathcal{A} = 1$, the bump is narrower and diffuses more in response to the noise. **E.** Variance of the bump as a function of time. Theory (solid line) given by Eq. (2.20) is compared with the results of 10^4 numerical simulations of Eq. (2.1). **F.** Diffusion coefficient computed as a function of \mathcal{A} . Theory (solid line) and sims (dots) compare favorably, showing a systematic decrease in diffusion as the strength of coupling \mathcal{A} is increased. Threshold $\theta = 0.25$ throughout, and $\omega_c = 25\pi/180$. Numerical simulations are performed using Euler-Maruyama stochastic integration scheme with $dx = 0.005$ and $dt = 0.1$.

in the space (x_1, x_2) satisfying $W(x_2 - x_1) = \theta$, which is precisely Eq. (2.10) in the case that $x_2 - x_1 = 2h$. Also, note that in the case that the interface locations are symmetric about $x = 0$, then $x_2(t) = -x_1(t) = a(t)$ can be described by a single equation by plugging into Eq. (2.17) to yield

$$\frac{da}{dt} = \frac{1}{\bar{\alpha}} (-\theta + W(2a(t))). \quad (2.18)$$

Lastly, note that we can examine the effects of noise by analyzing the stochastic differential equations

$$dx_1(t) = \frac{\theta - W(x_2(t) - x_1(t))}{\bar{\alpha}} dt - \frac{\sqrt{\epsilon \cdot \theta}}{\bar{\alpha}} dZ(x_1(t), t), \quad (2.19a)$$

$$dx_2(t) = \frac{-\theta + W(x_2(t) - x_1(t))}{\bar{\alpha}} dt + \frac{\sqrt{\epsilon \cdot \theta}}{\bar{\alpha}} dZ(x_2(t), t). \quad (2.19b)$$

As in previous work (Carroll et al, 2014; Kilpatrick and Ermentrout, 2013), we can track the stochastic motion of the bump's location by looking at the center of mass $\Delta(t) = (x_1(t) + x_2(t))/2$, evolving as

$$d\Delta(t) = \frac{\sqrt{\epsilon \cdot \theta}}{2\bar{\alpha}} [dZ(x_2(t), t) - dZ(x_1(t), t)],$$

which will have mean $\langle \Delta(t) \rangle = \Delta(0)$ and variance $\langle (\Delta(t) - \langle \Delta(t) \rangle)^2 \rangle = Dt$ with diffusion coefficient

$$\begin{aligned} D &= \frac{\epsilon\theta}{4\bar{\alpha}^2} \left[\langle Z(x_1, t)^2 \rangle + \langle Z(x_2, t)^2 \rangle - 2\langle Z(x_1, t)Z(x_2, t) \rangle \right], \\ &= \frac{\epsilon\theta}{2\bar{\alpha}^2} [C(0) - C(2h)], \end{aligned} \quad (2.20)$$

where $C(x)$ is a spatial correlation function. We derived a related equation in the case of additive noise by directly assuming stochastic motion of the bump's position in Kilpatrick and Ermentrout (2013).

We demonstrate the accuracy of these approximations by tracking the transient evolution of bumps in numerical simulations and comparing with predictions of Eq. (2.16). First, for a bump unforced by noise that is initiated with a narrower width than its equilibrium width, given by the wide solution to Eq. (2.10), the interfaces relax outward. In fact, these dynamics can be tracked by the interface Eq. (2.18), corresponding to the half-width of the evolving bump. We need only compute the integral Eq. (2.15) for our specific choice of weight function, Eq. (2.2):

$$W(x) = \mathcal{A} \int_0^x (1 - |y|) e^{-|y|} dy = \mathcal{A} x e^{-|x|}.$$

Thus, we can compute from Eq. (2.9) that

$$\bar{\alpha} = |U'_0(\pm h)| = \mathcal{A} \left[1 - (1 - 2h(\mathcal{A})) e^{-2h(\mathcal{A})} \right], \quad (2.21)$$

where the half-width depends on the spatial scale $h(\mathcal{A})$. In Fig. 4A,B, we compare the level sets $u(x_j(t), t) = \theta$ of a numerical simulation of Eq. (2.1) initiated with a narrower initial condition to the evolution of the interface Eq. (2.18), showing the expansion is tracked well. We also use Eq. (2.21) to approximate the evolution of noise-driven bumps, described by the stochastic interface Eq. (2.19). We use a cosine correlation function

$$C(x) = \cos(\omega_c x), \quad (2.22)$$

where $\omega_c = c\pi/L$, which sets the spatial scale of correlations. We demonstrate agreement between the prediction of our interface Eq. (2.19) and the level sets of Eq. (2.1) of a bump perturbed by noise in Fig. 4C,D. Furthermore, we can approximate the diffusion coefficient D corresponding to the rate at which the variance of the bump's centroid grows $\langle (\Delta(t) - \langle \Delta(t) \rangle)^2 \rangle = Dt$, as given by Eq. (2.20), so

$$D = \frac{\epsilon \theta}{2\mathcal{A}^2} \frac{1 - \cos(2\omega_c h)}{(1 + (2h(\mathcal{A}) - 1)e^{-2h(\mathcal{A})})^2}. \quad (2.23)$$

similar to results derived in Bressloff and Webber (2012); Kilpatrick and Ermentrout (2013). Fixing the noise amplitude ϵ , we find the diffusion coefficient decreases monotonically as the synaptic strength \mathcal{A} is increased (Fig. 4E,F). Thus, stronger synaptic inputs increase the size of the bumps, and these wider bumps are more stable to noise perturbations.

3 Dynamics of two interacting bumps

Our main interest lies in understanding how multiple bumps interact, so we can develop explicit formulas that describe the limitations of multi-item WM. Prior to examining WM for an arbitrary number of items, we focus on the case of two interacting bumps, to demonstrate how bump interactions lead to different errors during the delay period of a WM trial. Our effective equations derived here can be extended to higher dimensions.

3.1 Interface equations

We begin by extending our interface Eq. (2.16) for one bump to the case of two bumps. Again, since the nonlinearity in Eq. (2.1) is a step function $H(u - \theta)$, its output is determined by the active region $A(t) = \{x | u(x, t) \geq \theta\}$. In the case of a single bump, we defined a simply connected region as in Eq. (2.12). Two bumps would typically be comprised of two disjoint active regions. However, if the bumps began close enough together, their active regions would overlap and form a single connected domain. In this special case, the dynamics of the system would subsequently be described by the single bump interface Eq. (2.16). Thus, for our analysis here, we assume the active region is comprised of two disjoint subdomains, $A(t) = [x_1(t), x_2(t)] \cup [x_3(t), x_4(t)]$, so Eq. (2.1) becomes

$$du(x, t) = \left[-u(x, t) + \int_{x_1(t)}^{x_2(t)} w(x - y) dy + \int_{x_3(t)}^{x_4(t)} w(x - y) dy \right] dt + \sqrt{\epsilon \cdot |u(x, t)|} dZ(x, t). \quad (3.1)$$

As mentioned, we assume two bumps have been instantiated far enough apart so that their active regions do not overlap. Assuming continuity of $u(x, t)$, the boundary points of $A(t)$ correspond to the interfaces of the bumps, and satisfy the dynamic threshold equations

$$u(x_j(t), t) = \theta, \quad j = 1, 2, 3, 4. \quad (3.2)$$

Differentiating Eq. (3.2) with respect to t , we find the total derivative is again given by Eq. (2.13). Specifying the integral terms in Eq. (3.1) using Eq. (2.15), we can rewrite integrals as

$$\begin{aligned} \int_{x_1}^{x_2} w(x_j - y)dy + \int_{x_3}^{x_4} w(x_j - y)dy &= \int_{x_j - x_2}^{x_j - x_1} w(z)dz + \int_{x_j - x_4}^{x_j - x_3} w(x_j - y)dy \\ &= \sum_{k=1}^4 (-1)^{k-1} W(x_j(t) - x_k(t)). \end{aligned} \quad (3.3)$$

We study two cases of the two bump interface equations, which admit different approximations. For a fully deterministic Eq. (2.1), we can derive an integral equation for the time-evolution of the spatial gradients $\alpha_j(t)$ at the interfaces. An alternative approach, which is more straightforward, is to simply approximate the gradients $\alpha_j(t) \equiv \bar{\alpha}_j$ using static quantities derived from stationary solutions of Eq. (2.1). This is easier to employ, especially in the case of stochastic forcing.

Dynamic gradients. In the case of a fully deterministic system ($Z \equiv 0$ in Eq. (2.1)), we can follow Coombes et al (2012) to obtain an analytic formula for $\alpha_j(t)$ by defining $z(x, t) := \frac{\partial u(x, t)}{\partial x}$ and differentiating Eq. (3.1) with respect to x to find

$$\frac{\partial z(x, t)}{\partial t} = -z(x, t) + \sum_{k=1}^4 (-1)^{k-1} w(x - x_k(t)),$$

which we can integrate to yield

$$z(x, t) = e^{-t} \int_0^t e^s \left[\sum_{k=1}^4 (-1)^{k-1} w(x - x_k(s)) \right] ds + z(x, 0)e^{-t}. \quad (3.4)$$

Evaluating Eq. (3.4) at $x_j(t)$, we have:

$$\alpha_j(t) = e^{-t} \int_0^t e^s \left[\sum_{k=1}^4 (-1)^{k-1} w(x_j(t) - x_k(s)) \right] ds + \alpha_j(0)e^{-t}, \quad j = 1, 2, 3, 4. \quad (3.5)$$

Thus, we have a closed system describing the evolution of the interfaces of the two stationary bumps, assuming the active region $A(t)$ remains as two disjoint subdomains

$$\frac{dx_j}{dt} = -\frac{1}{\alpha_j(t)} \left[\sum_{k=1}^4 (-1)^{k-1} W(x_j(t) - x_k(t)) - \theta \right], \quad j = 1, 2, 3, 4, \quad (3.6)$$

with $\alpha_j(t)$ defined as in Eq. (3.5). The second order term in Eq. (2.13) will vanish, since there is no noise in this case. As we have performed no truncations, the pair of Eq. (3.5) and (3.6) exactly characterize the motion of the four bump interfaces (x_1, x_2, x_3, x_4) . We compare the evolution of the interfaces given by Eqs. (3.5) and (3.6) to those calculated from the full model Eq. (2.1) in Fig. 5A,B. Bumps can either move away from each other (Fig. 5A) or towards each other (Fig. 5B), depending on their initial distance Δ_x from one another. Note, merging occurs extremely rapidly, and repulsion happens otherwise. In our performance calculations, we account for this, and ignore the detailed dynamics of merging.

Note that for initial conditions that are symmetric about $x = 0$ ($x_4(0) = -x_1(0) = b(0)$ and $x_3(0) = -x_2(0) = a(0)$), the interfaces evolve symmetrically: $x_4(t) = -x_1(t) = b(t) \geq 0$ and $x_3(t) = -x_2(t) = a(t) \geq 0$. In a similar way, the dynamic gradients exhibit odd symmetry: $\alpha_1(t) = -\alpha_4(t) = \beta(t) \geq 0$ and $\alpha_3(t) = -\alpha_2(t) = \alpha(t) \geq 0$. Eqs. (3.5) and (3.6) can be reduced to four equations:

$$\frac{da(t)}{dt} = \frac{1}{\alpha(t)} [\theta - W(b(t) - a(t)) + W(2a(t)) - W(a(t) + b(t))], \quad (3.7a)$$

$$\frac{db(t)}{dt} = \frac{1}{\beta(t)} [W(b(t) - a(t)) - \theta + W(2b(t)) - W(a(t) + b(t))], \quad (3.7b)$$

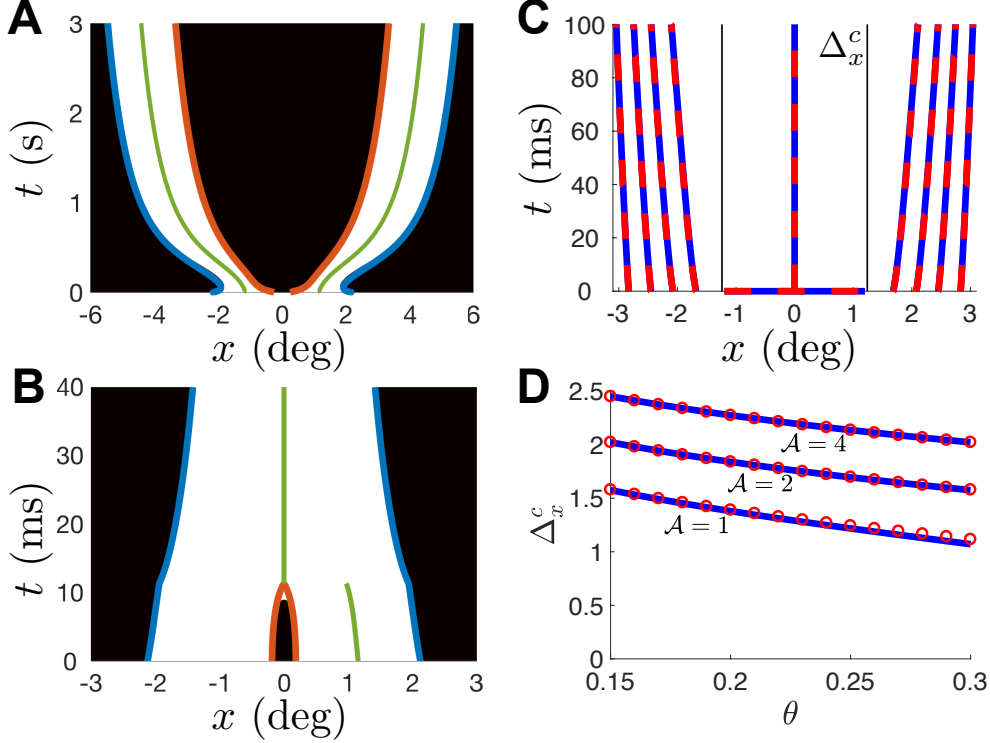


Fig. 5 Two bumps interacting in the deterministic ($Z \equiv 0$) neural field Eq. (2.1). **A.** Two bumps repel each other when initiated at $\pm x_0 = \pm 1.25$. The location of the bump interfaces are well-tracked by the curves (solid lines) generated by the low-dimensional Eq. (3.7). Parameters are $\theta = 0.25$ and $\mathcal{A} = 1$. **B.** Two bumps merge when initiated at $\pm x_0 = \pm 1.23$, a short distance for the point of initiation in **A**. **C.** Multiple trajectories of the centroid of the bump for initial conditions $x_0 = \{1.2, 1.6, 2.0, 2.4, 2.8\}$ as predicted by Eq. (3.7) (solid line) and direct simulation (dashed lines). Bumps repel each other more strongly when they begin close to the critical boundary Δ_x^c (thin line). Within the critical boundary, bumps merge. **D.** The critical boundary $\Delta_x^c(\theta)$ is determined by Eq. (3.8) (solid curves), and compared with direct simulations (circles). See Fig. 4 for details on numerical simulations.

$$\alpha(t) = e^{-t} \int_0^t e^s [w(a(t) + b(s)) - w(a(t) + a(s)) + w(a(t) - a(s)) - w(a(t) - b(s))] ds + \alpha(0)e^{-t}, \quad (3.7c)$$

$$\beta(t) = e^{-t} \int_0^t e^s [w(b(t) + a(s)) - w(b(t) + b(s)) + w(b(t) - b(s)) - w(b(t) - a(s))] ds - \beta(0)e^{-t}. \quad (3.7d)$$

The system, Eq. (3.7), is used to calculate the interfaces of the two scenarios shown in Fig. 5A,B.

There is a critical distance Δ_x^c , which divides solutions that drift apart ($\Delta_x > \Delta_x^c$) from those that are attracted to each other ($\Delta_x < \Delta_x^c$). We illustrate this by tracking the centroids of two symmetrically placed bumps for various starting distances Δ_x (Fig. 5C). Similar features of associated spiking network models have been identified in Almeida et al (2015); Wei et al (2012). We can determine an analytical expression that accurately characterizes the critical distance Δ_x^c . Utilizing Eq. (3.7a), we note that if $a'(t) < 0$, bumps will initially move towards one another. Motivated by the findings of our numerical simulations in Fig. 5C, we expect bumps that are initially attracted will continue to move towards one another until they merge. In this case, the critical curve (a^c, b^c), determined by the condition

$$\theta = W(b^c - a^c) + W(2a^c) - W(a^c + b^c) \quad (3.8)$$

divides initial conditions ($a(0), b(0)$) that merge from those that repel each other. Assuming the bumps initially have width $b(0) - a(0) = 2h$, as prescribed by Eq. (2.9), then $\theta = W(b(0) - a(0))$ and Eq. (3.8) simplifies to $W(2a^c) = W(a^c + b^c)$. We compare the prediction of Eq. (3.8) to the results of numerical simulations, and find they match remarkably well (Fig. 5D). Thus, our interface equations not only track the motion of bumps, but can also predict when they merge with one another.

Static gradient approximation. An alternative to computing the integral equations in Eq. (3.5) is to assume a static approximation to the gradients $\alpha_j(t) \equiv \bar{\alpha}_j$. Since our solutions evolve with a profile approximated by sums of the stationary bump solution $U_0(x)$, Eq. (2.5), we consider gradients approximated by

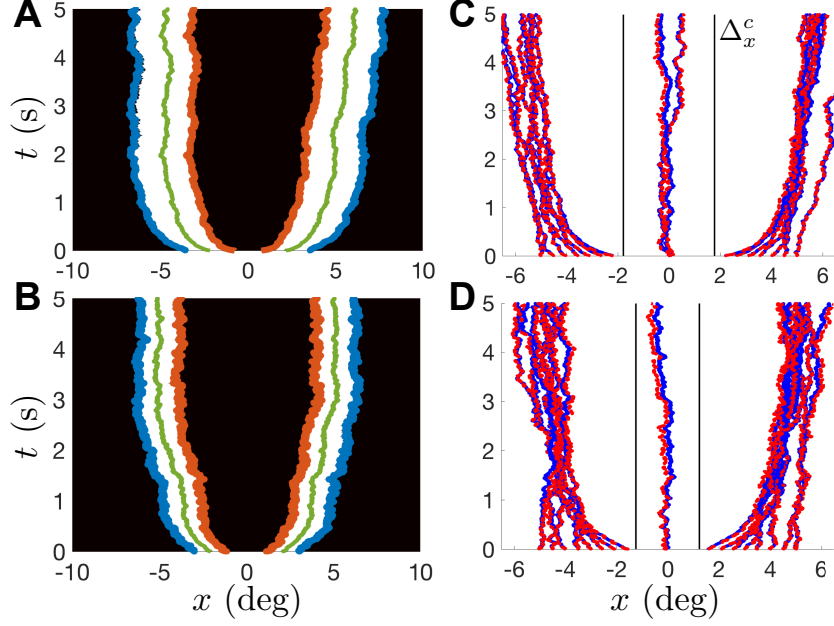


Fig. 6 Stochastic simulations of Eq. (2.1) with noise amplitude $\epsilon = 0.03$ and noise correlations, Eq. (2.22). **A.** Two noise-driven bumps repel each other and diffuse when starting at $\pm x_0 = \pm 2$. Our estimate using the static gradient approximation (solid lines), Eq. (3.9), tracks the interfaces. Other parameters are $\theta = 0.25$ and $\mathcal{A} = 2$. **B.** When $\mathcal{A} = 1$, the bumps repel each other less, and stray less from their initial position than in **A**. **C.** Trajectories of the centroid of the noise-driven bumps initiated at different locations $\pm x_0$ from 1 to 5 deg, spaced 0.5 deg apart. Approximations (solid lines) using the low-dimensional system, Eq. (3.10), agree with direct numerical simulations (dashed lines). When initiated within the region $x_0 < \Delta_x^c$ (thin lines), bumps merge as in the deterministic Fig. 5. Here, $\mathcal{A} = 2$. **D** Same as **C**, except $\mathcal{A} = 1$, showing bumps repel each other less and also merge in a narrower range. See Fig. 4 for details on numerical simulations.

$U'_0(x)$. For the weight function Eq. (2.2), these can be computed directly from Eq. (2.21) as

$$\bar{\alpha}_{1,3} = -\bar{\alpha}_{2,4} = \bar{\alpha} = U'_0(-h).$$

We can then write the resulting interface equations in a simple form that still captures the interactions between the two bumps, as well as the effects of noise perturbations:

$$dx_1 = \frac{1}{\bar{\alpha}} \left([\theta - W(x_2 - x_1) + W(x_3 - x_1) - W(x_4 - x_1)] dt - \sqrt{\epsilon \cdot \theta} dZ(x_1, t) \right), \quad (3.9a)$$

$$dx_2 = -\frac{1}{\bar{\alpha}} \left([\theta - W(x_2 - x_1) + W(x_3 - x_2) - W(x_4 - x_2)] dt - \sqrt{\epsilon \cdot \theta} dZ(x_2, t) \right), \quad (3.9b)$$

$$dx_3 = \frac{1}{\bar{\alpha}} \left([\theta - W(x_4 - x_3) + W(x_3 - x_2) - W(x_3 - x_1)] dt - \sqrt{\epsilon \cdot \theta} dZ(x_3, t) \right), \quad (3.9c)$$

$$dx_4 = -\frac{1}{\bar{\alpha}} \left([\theta - W(x_4 - x_3) + W(x_4 - x_2) - W(x_4 - x_1)] dt - \sqrt{\epsilon \cdot \theta} dZ(x_4, t) \right). \quad (3.9d)$$

As in the case of single-bumps, the second order term in Eq. (2.13) is smaller than $\mathcal{O}(\sqrt{\epsilon})$. The system Eq. (3.9) yields an accurate approximation of the stochastic dynamics of the two bumps' interfaces (Fig. 6A,B). We can also reduce Eq. (3.9) to track the centroid of each bump $\Delta_1 = (x_1 + x_2)/2$ and $\Delta_2 = (x_3 + x_4)/2$. To do so, we assume the width of each bump remains approximately constant, so $x_1 = \Delta_1 - h$, $x_2 = \Delta_1 + h$, $x_3 = \Delta_2 - h$, and $x_4 = \Delta_2 + h$. In this case, we find two equations for the stochastic dynamics of the centroids:

$$d\Delta_1 = \frac{1}{\bar{\alpha}} \left(J(\Delta_2 - \Delta_1) dt + \frac{\sqrt{\epsilon \cdot \theta}}{2} dZ(\Delta_1, t) \right), \quad (3.10a)$$

$$d\Delta_2 = \frac{1}{\bar{\alpha}} \left(-J(\Delta_2 - \Delta_1) dt + \frac{\sqrt{\epsilon \cdot \theta}}{2} dZ(\Delta_2, t) \right), \quad (3.10b)$$

where

$$J(\Delta) = \frac{1}{2} (W(\Delta) - W(\Delta - 2h) - W(\Delta + 2h)),$$

$$dZ(\Delta_j, t) = dZ(\Delta_j - h, t) - dZ(\Delta_j + h, t), \quad j = 1, 2.$$

We use the approximation, Eq. (3.10), to determine the evolution of the centroids in realizations with different initial conditions (Fig. 6C,D). Even though the bump for $\mathcal{A} = 2$ has a lower diffusion coefficient (as shown in Fig. 4E,F), for $\mathcal{A} = 1$, bumps repel each other less. Thus, weaker synaptic weights may confer more of an advantage when bumps are initiated close together, since initial conditions are better preserved. However, when bumps begin far apart, strong connectivity may be more advantageous, since bumps are less perturbed by noise. We examine this tradeoff by determining performance of the network in a two-item WM task, using our approximations and full numerical simulations.

3.2 Performance

We study estimation errors of the network encoding locations of two targets, ϕ_1 and ϕ_2 . In general, we categorize errors as arising from (a) merging; (b) repulsion; and (c) diffusion. The fluctuation-driven random walk of bumps has been characterized in single-item WM models (Compte et al, 2000; Kilpatrick and Ermentrout, 2013), and validated in behavioral and electrophysiological experiments (Constantinidis and Klingberg, 2016; Wimmer et al, 2014). Bump merging was recently characterized in spiking network models of multi-item WM (Almeida et al, 2015; Wei et al, 2012), motivated by corresponding human psychophysics data (Bays et al, 2009). The merging of item memories has been considered in heuristic models of multi-item WM, and authors sometimes assume that the memory for one of the associated items is then completely lost, so subjects guess to report its location (Zhang and Luck, 2008). Similar guesses may occur due to attentional lapses, where subjects do not store an item in the first place. We avoid such characterizations in our analysis, and study error solely ascribed to the dynamics of the bump attractor network, Eq. (2.1). Thus, we assume that when bumps merge, the remaining bump encodes the location of both items corresponding to the original two bumps. Finally, note that repulsion will lead to item memories that diverge from one another when bumps are instantiated close to one another.

Across multiple trials, the task on trial k is to encode both target angles $\phi_1^k, \phi_2^k \in [-180, 180)$ ($\phi_1^k < \phi_2^k$). However, only a single target is probed, for instance by asking the subject to recall the angle corresponding to a particular color (Bays et al, 2009; Wilken and Ma, 2004; Zhang and Luck, 2008). Due to the symmetry in the system, we compute the mean squared error (MSE) corresponding to the first target angle ϕ_1^k on each trial k

$$\text{MSE} = \langle (\Delta_{1\text{-out}} - \phi_1)^2 \rangle = \frac{1}{K} \sum_{k=1}^K (\Delta_{1\text{-out}}^k - \phi_1^k)^2, \quad (3.11)$$

where $\Delta_{j\text{-out}}^1$ is the centroid of the bump encoding target 1 at the end of the trial k (as in Fig. 7A,D). The MSE in Eq. (3.11) can be computed directly from numerical simulations of Eq. (2.1), and we can also approximate the error using our reduced set of centroid equations, Eq. (3.10).

Our approximation of the MSE begins by determining whether or not the bumps merge. To do so, we examine the target distance to see if it is below the critical value, $(\phi_2 - \phi_1) < 2\Delta_x^c$ (Fig. 5D). As shown in Fig. 5B, merging occurs very rapidly, so we do not model the detailed dynamics of merging in our performance calculations. Leveraging Eq. (3.8), which describes the minimal distance at which symmetrically-placed bumps do not merge, we rotate coordinates of $\phi_{1,2}$ so they are symmetric about zero $\tilde{\phi}_{1,2} = (\phi_1 - \phi_2, \phi_2 - \phi_1)/2$. Thus, in Eq. (3.8), assuming the initial bumps are roughly of width $2h$ we have $a^c = (\phi_2 - \phi_1 - 2h)/2$ and $b^c = (\phi_2 - \phi_1 + 2h)/2$, so if $W((\phi_2 - \phi_1 - 2h)/2) < W(\phi_2 - \phi_1)$, the bumps merge, otherwise they repel each other. This boundary is approximated given the weight function, Eq. (2.2), by solving the corresponding equality, $\phi_2 - \phi_1 = \frac{2h}{1 - e^{-2h}}$, as the critical distance below which bumps merge. For this subset of cases, the MSE in Eq. (3.11) can be approximated in a straightforward way by noting

$$\begin{aligned} \text{MSE}_{\text{merge}} &= \langle (\Delta_{1\text{-out}} - \phi_1)^2 \rangle = \langle (\Delta_{1\text{-out}} - (\phi_1 + \phi_2)/2 - (\phi_1 - \phi_2)/2)^2 \rangle \\ &\approx \langle (\Delta_{1\text{-out}} - (\phi_1 + \phi_2)/2)^2 \rangle + \langle (\phi_1 - \phi_2)^2/4 \rangle = D \cdot T + \frac{(\phi_2 - \phi_1)^2}{4}, \end{aligned} \quad (3.12)$$

since the merged bump rapidly centers at the mean of the two target locations, $(\phi_1 + \phi_2)/2$. We can compute the diffusion coefficient D using Eq. (2.23), our theory for the stochastic dynamics of single bumps, and T is the total delay time.

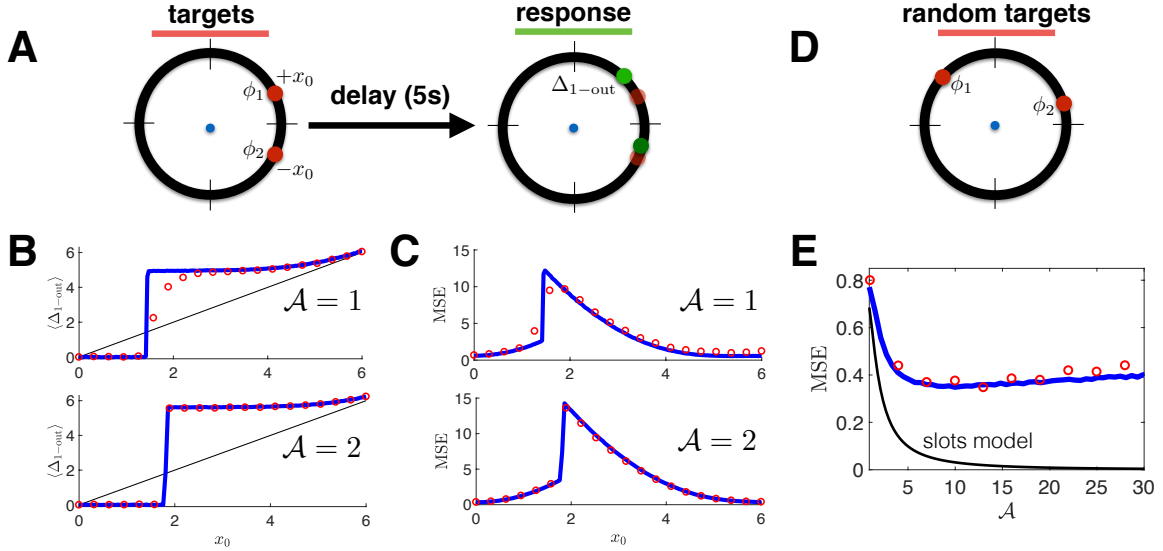


Fig. 7 Recall error in a two-item WM task. **A.** Item-distance dependence of errors. Target items $\phi_{1,2}$ are located at $\pm x_0$. Mean squared error (MSE) is computed by comparing output angle Δ_{1-out} to input ϕ_1 via Eq. (3.11). **B.** Mean location of Δ_{1-out} computed as a function of x_0 for low-dimensional Eq. (3.10), (solid lines), and full simulations of the neural field (circles). Merging leads to values close to zero. A transition occurs at the boundary of merging, where repulsion begins. For large enough x_0 , $\langle \Delta_{1-out} \rangle \approx +x_0$. Compare $\mathcal{A} = 1$ and $\mathcal{A} = 2$. **C.** MSE as a function of x_0 computed from Eq. (3.11) is maximized near the boundary point, where repulsion is strongest, decreasing as the bumps are placed further apart. **D.** MSE is also computed for uniform random targets $\phi_{1,2}$, averaging across all locations to compute the MSE for each synaptic strength \mathcal{A} . **E.** MSE is nonmonotonic in \mathcal{A} , with fluctuation-driven errors dominating for low \mathcal{A} and merging/repulsion errors dominating for large \mathcal{A} . MSE is much larger would be predicted for a slots model, which assumes MSE unchanged between one and two item memory tasks. All curves and circles are generated from 10^6 Monte Carlo simulations.

If bumps do not merge, we approximate their dynamics using the nonlinear stochastic system, Eq. (3.10). The constituent function $J(\Delta)$ can be computed, given the weight function, Eq. (2.2),

$$J(\Delta) = -\mathcal{A}e^{-\Delta} \left[2\Delta \sinh^2(h) - 2h \sinh(2h) \right],$$

assuming $\Delta > 0$. Note, the formula for $J(\Delta)$ is more complicated for the case in which $\Delta_2 < \Delta_1$, or their difference is across the periodic boundary at $x = \pm 180$. We consider these other cases in simulations, but do not discuss the formulas in detail here. In the case of noise correlations, Eq. (2.22), we can specify

$$d\mathcal{Z}(\Delta_j, t) = 2 \sin(\omega_c h) [\sin(\omega_c \Delta_j) \cdot d\xi_1(t) - \cos(\omega_c \Delta_j) \cdot d\xi_2(t)],$$

where $d\xi_j(t)$, $j = 1, 2$, are increments of a standard Wiener process. Eq. (3.10) is simulated numerically to estimate Δ_{1-out}^k and Δ_{2-out}^k in trial k , which then is plugged into our formula for MSE, Eq. (3.11).

Our approximations are compared to simulations of the full neural field model, Eq. (2.1), in Fig. 7. Targets angles ϕ_1 and ϕ_2 are initially represented by instantiating a bump of form $U_0(x)$, Eq. (2.9), centered at the two locations in the neural field. Distance-dependence is considered first (Fig. 7A), and then trials with random initial angles are considered (Fig. 7D). The system evolves for $T = 5s$ (500 time units), and then the centroid of the bumps corresponding to ϕ_1 is read out and compared to the original angle by computing Eq. (3.11). If the bumps merge, both items are represented by the remaining bump. The MSE is similarly computed using the low-dimensional approximation, Eq. (3.10), if the bumps begin sufficiently far apart, otherwise Eq. (3.12) is used to approximate the MSE. These approximations are compared to the full simulations in Fig. 7B,C, for the case in which the initial target angles are $\phi_1 = +x_0$ and $\phi_2 = -x_0$. Merging causes both bumps to have mean position $x = 0$, when the initial targets $\pm x_0$ are sufficiently close (Fig. 7B). Beyond this boundary, the stored angles repel one another. There is an abrupt transition in the MSE corresponding to this boundary point (Fig. 7C). Importantly, the MSE is limited from below by the variance a single bump ($\langle \Delta^2 \rangle = D \cdot T$), not interacting with another bump. Additional contributions to the MSE arise from bump interactions.

Performance on the two-item WM task with random initial targets ϕ_1 and ϕ_2 is considered in Fig. 7E. Unlike a slots model of multi-item WM (Cowan, 2010; Zhang and Luck, 2008), recall variability, represented by the MSE, is greater than predicted by a single-item store. Both items (bumps) are stored in

a single network, producing interactions between bumps when items are initially close, which contributes an additional source of variability to the recall. Merging produces a systematic shift in the remembered location of items, as does repelling. The frequency of these interactions grows as the synaptic strength parameter \mathcal{A} is increased, counteracting the reduction in diffusion also produced by increasing \mathcal{A} . This tradeoff produces a non-monotonic dependence of the MSE on \mathcal{A} (Fig. 7E), so there is an optimal \mathcal{A} for two-item storage with low-diffusion of bumps and low-probability of bump interaction. Note, the MSE in the interacting bumps model is larger than would be predicted by a slots model that assumes MSE is unchanged as the number of items is increased up to some fixed capacity.

Our interacting bumps model can account for the item-dependent increase in the variability of recall in two-item WM tasks (Bays et al, 2009; Wilken and Ma, 2004). This arises due to the nonlinear interactions between the bumps, which add to the variability already present due to the dynamic fluctuations in the network. We now examine item-dependent changes in recall variability for tasks with more than two items, showing our analysis extends to the case of multiple interacting bumps.

4 Multiple interacting bumps

Recent models of multi-item WM focus on uncovering the nature of item-number limitations, as they impact response variability (Ma et al, 2014). Phenomenological models can be altered to capture errors that either reflect a finite capacity or the distribution of resources (Zhang and Luck, 2008), but physiologically-inspired models account for the architecture and dynamics of neural circuits underlying WM storage (Bays, 2015). The work of Almeida et al (2015); Wei et al (2012) has shown that a recurrent spiking network can support multiple bumps that each individually encode a different item. Our model is a tractable version of these previous studies, allowing us to derive explicit expressions describing limitations of the network.

Prior to developing effective equations for bump interfaces, we consider the problem of network capacity. This is one way in which our model differs from the standard resource model of WM. Only a finite number of bumps can be stored in the recurrent network, and this upper limit is determined by the choice of the synaptic strength parameter \mathcal{A} . However, we note this upper limit is quite large. We can approximate this limit by again examining a stationary solution problem.

4.1 Network capacity

We frame the problem of identifying network capacity by attempting to identify multi-bump stationary solutions to Eq. (2.1) in the absence of noise ($Z \equiv 0$). Finite multi-bump solutions are not stable in the limit $L \rightarrow \infty$ (Laing and Troy, 2003b), since multiple active regions exert a repulsive drift on one another. If bumps are spaced evenly around the domain, the conformation is stable since the repulsive forces acting on each bump from either direction balance. Thus, stable multi-bump solutions constitute a periodic pattern that wraps around the domain. One question is just how the minimal period of this pattern changes as the synaptic strength \mathcal{A} is changed. Since \mathcal{A} increases the width of single bump solutions, one might expect the capacity to decrease as \mathcal{A} is increased. We demonstrate in fact that the capacity of the network grows as the synaptic strength \mathcal{A} is increased (Fig. 8A).

Network capacity can be bounded by examining the upper limit on the number of possible bumps in a periodic solution to Eq. (2.1). These numbers will tend to be much larger than those imposed by a slots model of WM capacity (Zhang and Luck, 2008), so our model will still behave approximately as an infinite resource model since the capacity $N_{\mathcal{A}}$ is quite high. The capacity can be estimated by studying the existence of multi-bump solutions, comprised of multiple stationary active regions of the same width, spaced an even distance apart. For example, a two-bump solution with centroids at $x = \pm 90$ has the form

$$U(x) = \int_{-90-h_2}^{-90+h_2} w(x-y)dy + \int_{90-h_2}^{90+h_2} w(x-y)dy.$$

As in the case of single bumps, there is one unknown, which is the half-width of each bump h_2 . Self-consistency of the threshold conditions $U(-90 \pm h_2) = U(90 \pm h_2) = \theta$ yields an implicit equation

$$\theta = \int_0^{2h_2} w(y)dy + \int_{180-2h_2}^{180} w(y)dy, \quad (4.1)$$

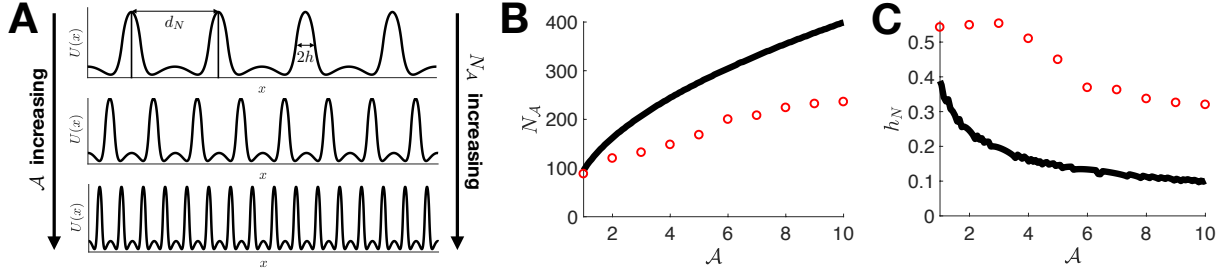


Fig. 8 Capacity of the network, Eq. (2.1), is upper bounded by the number of stable bumps $N_{\mathcal{A}}$ that can be instantiated in the periodic domain $x \in [-180, 180)$. **A.** We find the capacity tends to increase with synaptic strength \mathcal{A} , since stronger synapses lead to narrower bumps in multibump solutions. **B.** The maximal number $N_{\mathcal{A}}$ of bumps that can be packed into the domain increases with \mathcal{A} . Periodic bump solutions have spacing $d_N = 360/N$ between centroids, and the same half-width h_N for each bump. Solid line shows result from theory Eq. (4.4), circles are results from numerical simulations (See main text). **C.** The bump half-width h_N associated with the maximal capacity solution narrows for increasing synaptic strength \mathcal{A} owing to the strong recurrent inhibition for networks with large \mathcal{A} . Threshold $\theta = 0.25$.

which follows from the periodicity of the weight function ($w(180 + \alpha) = w(180 - \alpha)$). Computing integrals in Eq. (4.1) for the weight function Eq. (2.2), we find the implicit equation for the half width h_2 is

$$\theta = 2\mathcal{A} \left(h_2 e^{-2h_2} + e^{-180} \left[90 - (90 - h_2) e^{2h_2} \right] \right), \quad (4.2)$$

so if Eq. (4.2) has a solution we expect the network with synaptic strength \mathcal{A} to have capacity of at least two items. Note $e^{-180} \approx 6.17 \times 10^{-79}$ is extremely small, so networks in which single bumps exist will likely also possess two bump solutions, since Eq. (4.2) is a very mild perturbation of Eq. (2.10). This approach can be generalized to the case of more than two bumps ($N > 2$), yielding analogous equations to Eq. (4.2) for the associate bump half-width.

Solutions with N distinct bumps have a regular spacing between each of the bump, forming a periodic pattern that tiles the domain. The spacing between the centroid of each bump is computed by partitioning the domain by N , $d_N = 360/N$. We can write an N -bump solution in the form

$$U(x) = \sum_{j=1}^N \int_{c_j - h_N}^{c_j + h_N} w(x - y) dy$$

where $c_j = -180 + (j + 1/2)d_N$ is the location of the centroid of the j^{th} bump. Threshold conditions $U(c_j \pm h_N) = \theta$ for $j = 1, \dots, N$ yield the implicit equation for the half-width

$$\theta = \sum_{j=0}^{N-1} \int_{jd_N}^{jd_N + 2h_N} w(y) dy. \quad (4.3)$$

For N large, Eq. (4.3) will contain many very small terms corresponding to the interactions between distant bumps. It is easier to express the sum of integrals in Eq. (4.3) by approximating the N -bump solution on $x \in [-180, 180)$ with an infinite-bump solution on $x \in (-\infty, \infty)$. Placing the core bump at $x = 0$, and other bumps with centroids at jd_N for j a nonzero integer, yields the implicit equation

$$\theta = \sum_{j=-\infty}^{\infty} \int_{jd_N}^{jd_N + 2h_N} w(y) dy,$$

which we can integrate directly using the weight function Eq. (2.2), resulting in the following equation that must be solvable for a neural field on $x \in (-\infty, \infty)$ to have periodic bump solutions spaced d_N apart:

$$\theta = \mathcal{A} \left(2h_N e^{-2h_N} + \mathcal{S}(h_N, d_N) \right), \quad (4.4)$$

where

$$\mathcal{S}(h, d) = \sum_{j=1}^{\infty} e^{-jd} [4h \cosh(2h) - 2jd \sinh(2h)],$$

$$= \frac{4h \cosh(2h)}{e^d - 1} - \frac{2de^d \sinh(2h)}{(e^d - 1)^2}.$$

We also require $h_N \in [0, d_N/2)$, since the active region of each bump cannot overlap with another. Thus, the capacity $N_{\mathcal{A}}$ is approximated by the maximum value N for which Eq. (4.4) possesses a solution. We plot $N_{\mathcal{A}}$ as a function of \mathcal{A} in Fig. 8B (solid line), showing the capacity is an increasing function of synaptic strength. This may seem surprising, since one might expect that bumps will be wider as \mathcal{A} grows. However, this is only true when inter-bump interactions are not considered. Many bumps will tend to interact through strong inhibition, which narrows them, decreasing h_N (Fig. 8C), but they will still be sustained by the strong recurrent excitation generated by increasing \mathcal{A} .

Due to both the infinite domain approximation in Eq. (4.4) and inevitable truncation errors in our numerical root-finding scheme, we find that the maximal number of bumps predicted by our theory overestimates what we find in numerical simulations (circles in Fig. 8B,C). Recall, we are identifying roots of a transcendental equation, which can be quite sensitive to truncation errors. Thus, in practice we would certainly not expect the capacity predicted by our theory to be obtained in simulations of Eq. (2.1) with stochastic forcing. While calculations using Eq. (4.4) provide a clean method for estimating the upper bound on bump number in the network, in practice, we expect these solutions to be sensitive to perturbations arising in a numerical integration scheme (See for example discussion in Guo and Chow (2005)). Therefore, we also performed a coarser estimate of the network capacity by using a simple numerical simulation method, to find how many bumps can be packed into the domain $x \in [-180, 180)$ for each \mathcal{A} . We ran numerical simulations of Eq. (2.1) in the absence of noise with the initial condition $u(x, 0) = \sin(N\pi x/180)$, allowing them to equilibrate after long time ($t \rightarrow 5s$). At this point, we counted the number of bumps remaining, and computed their half-width, plotting the result in comparison to our analysis in Fig. 8B,C (circles). In fact, this method provides a considerably lower bound on the estimate, but the trend of the maximum bump number increasing with \mathcal{A} is still present.

We now examine dynamic interactions of bumps in numerical simulations of Eq. (2.1) for the case of a more than two bumps, and derive a low-dimensional system for the interface dynamics.

4.2 Interface equations

We extend the interface equations derived for the interactions of two bumps to account for interactions between an arbitrary number of bumps in the network. As in the case of two bumps, if multiple bumps' initial active regions overlap, they will merge. This sets an upper bound on the capacity of the network (as in Fig. 8). Our analysis proceeds now by projecting the dynamics of bumps in the network to equations that simply track bump interfaces.

The active region in this case is given by the union of N finite intervals, which we assume to be disjoint, $A(t) = \cup_{j=1}^N [a_j(t), b_j(t)]$. Note, in the case that bumps' active regions overlap, we simply redefine a set of fewer than N finite intervals, with some corresponding to the merged bumps. In the case of N distinct active regions, Eq. (2.1) becomes

$$du(x, t) = \left[-u(x, t) + \sum_{j=1}^N \int_{a_j(t)}^{b_j(t)} w(x - y) dy \right] dt + \sqrt{\epsilon \cdot |u(x, t)|} dZ(x, t).$$

The dynamic threshold equations are then given

$$u(a_j(t), t) = u(b_j(t), t) = \theta, \quad j = 1, \dots, N. \quad (4.5)$$

As before, we differentiate Eq. (4.5), rewrite the corresponding integrals using Eq. (2.15), and assume the gradients at the threshold are static and approximated by the stationary bump gradients ($\bar{\alpha} = U'_0(-h)$). We can approximate the interface dynamics by the following stochastic system:

$$da_j = \frac{1}{\bar{\alpha}} \left(\left[\theta - \sum_{k=1}^N (W(a_j - a_k) - W(a_j - b_k)) \right] dt - \sqrt{\epsilon \cdot \theta} dZ(a_j, t) \right), \quad (4.6a)$$

$$db_j = -\frac{1}{\bar{\alpha}} \left(\left[\theta - \sum_{k=1}^N (W(b_j - a_k) - W(b_j - b_k)) \right] dt - \sqrt{\epsilon \cdot \theta} dZ(b_j, t) \right), \quad (4.6b)$$

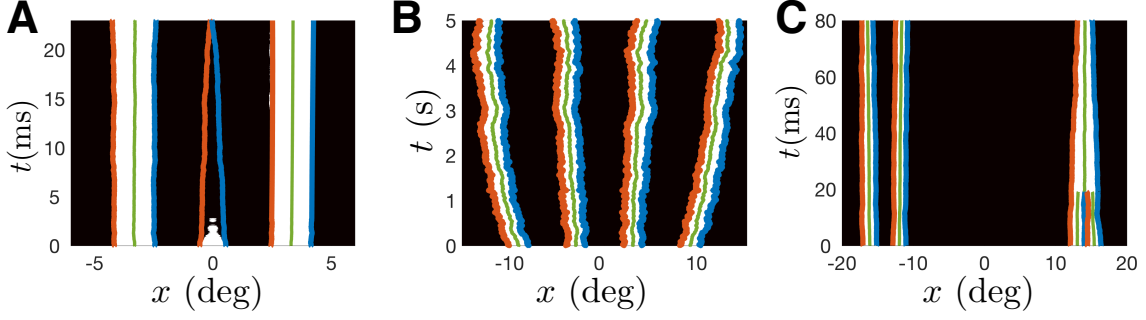


Fig. 9 Categories of bump interactions that induce WM errors. **A.** Annihilation occurs when a bump is closely flanked by two others, leading to extinction of the inner bump. **B.** Repulsion drives bumps away from one another, due to the recurrent inhibition acting at long distances. **C.** Bumps will merge if two begin close and are not in the vicinity of other bumps. Interface equations, Eq. (4.6), track the dynamics of full numerical simulations of Eq. (2.1). Parameters are $\epsilon = 0.03$ and $\theta = 0.25$.

for $j = 1, \dots, N$. Furthermore, the dynamics of the centroid of each bump j can be tracked by using the change of variables, $\Delta_j = (a_j + b_j)/2$, along with the approximations $a_j \approx \Delta_j - h$ and $b_j \approx \Delta_j + h$, yielding the system of N stochastic differential equations

$$d\Delta_j = \frac{1}{\alpha} \left(\sum_{k=1, k \neq j}^N J(\Delta_k - \Delta_j) dt + \frac{\sqrt{\epsilon \cdot \theta}}{2} dZ(\Delta_j, t) \right), \quad (4.7)$$

for $j = 1, \dots, N$, where $J(\Delta)$ and $dZ(\Delta_j, t)$ are defined as in Eq. (3.10). While we could employ the low-dimensional approximation, Eq. (4.7), to approximate how the network, Eq. (2.1), performs on multi-item WM tasks, we opt to preserve the interface information in Eq. (4.6). Interactions between multiple bumps are much better captured when the width of bumps is also considered along with their position. Truncating to only consider the centroid, removes the perturbations of width from the low-dimensional dynamics, which for example ignores the possibility of bump annihilation events.

We demonstrate the efficacy of the low-dimensional description, Eq. (4.6) in capturing the dynamics of the bump interfaces in Fig. 9. One category of dynamics that is much more common in the case of multiple bumps is annihilation of a bump by two neighboring bumps on either side (Fig. 9A). Notice, the middle bump does not merge with the bump on the left or right, but is extinguished by their combined recurrent inhibition. This is captured reasonably well by our interface Eq. (4.6). Note, annihilation events can also occur in the case of two bumps being instantiated close to one another. The combination of noise and lateral inhibition can lead to one bump's extinction without it merging with the neighboring bump. Bump edges fluctuate in response to noise, and multiple bumps can collectively repel each other when they are not too close (Fig. 9B). Merging occurs when two bumps begin close to one another, but are not in the vicinity of other bumps (Fig. 9C).

4.3 Performance

Estimation errors for tasks of encoding an arbitrary number of targets N , $\{\phi_1, \phi_2, \dots, \phi_N\}$, still mostly arise from merging, repulsion, or diffusion. However, recurrent inhibition from multiple active regions can also result in annihilation of bumps, so the activity is extinguished separately from a neighboring bump (as shown in Fig. 9A). These errors combine to shape the response variability, measured by the MSE in Eq. (3.11), as a function of the item number N . Our results demonstrate much more consistency with a resource model of multi-item WM. In particular, we see that the response variability for individual items increases with the number of items stored in memory, starting with the difference between $N = 1$ and $N = 2$ discussed in the previous section (Fig. 7E).

We have to make specific choices about how multiple bumps encode the multiple target items that initially instantiate them. As in the case of two-items, we ignore probabilistic effects that could further contribute to the error beyond that captured by the stochastic dynamics of the bumps (Bays et al, 2009). Lapses and swaps are not considered in our model. When two bumps merge with one another, or one bump is annihilated, the items associated with vanishing bumps are then associated to the closest remaining bump.

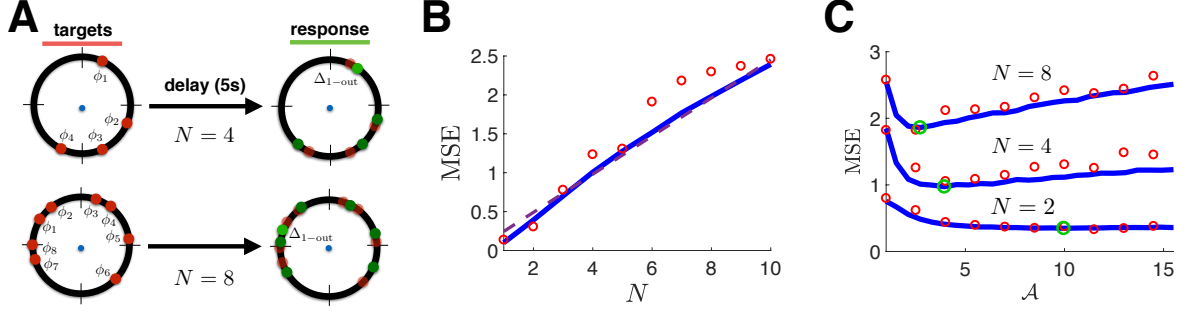


Fig. 10 Recall error in multi-item WM task. **A**. There are N target items $\{\phi_1, \phi_2, \dots, \phi_N\}$ whose locations are chosen uniformly randomly around $x \in [-180, 180]$. Mean squared error (MSE) is computed by comparing the output angle Δ_{1-out} of a randomly chosen input ϕ_1 via Eq. (3.11). **B**. MSE increases with the number of items N , computed from Eq. (4.6), (solid line), agreeing with numerical simulations of Eq. (2.1), (circles). Trend is fit by a linear function (dashed line). We fix $A = 5$. **C**. MSE is nonmonotonic in synaptic strength A , owing to the tradeoff between fluctuation-driven errors (at small A), and bump interaction errors (at large A). Note, the optimal A (large circles) decreases as N is increased.

Handling bump annihilation events parsimoniously singles out the contributions to the error engendered solely by the neural circuit dynamics described by our recurrent network.

The MSE of a single item is computed using the formula, Eq. (3.11), as before. Recall, we assume that a subject is probed about a single item in WM, as this is the protocol typical used to measure behavioral errors (Ma et al, 2014). Furthermore, this allows us to significantly reduce the space of dynamics that we must track in each numerical simulation. Rather than having to track the locations of all bumps, it is sufficient to only follow the dynamics of bumps in the vicinity of the bump originating from the item of interest. We will examine performance when target angles $\{\phi_1, \phi_2, \dots, \phi_N\}$ are randomly placed about the domain $x \in [-180, 180]$ (Fig. 10A). First, we examine the scaling of recall variability, measured by MSE, as a function of the number of items stored N . As expected by our two-bump performance results, we find that the MSE grows steadily with N (Fig. 10B). This is suggestive of the resource model of WM, since the increase occurs across all N . Next, we study the effect of varying the synaptic strength A for different item number counts. Extending our findings for two-item memory, we see there is an optimal A that minimizes the MSE, and this optimum decreases as N is increased. Thus, as more items must be stored in the network, it is more advantageous to have networks with narrower bumps to decrease the probability of bump interactions.

We conclude that an interacting bumps model of multi-item WM can capture several key features of error. Synaptic fluctuations lead to the time-dependent scaling typically observed in parametric WM tasks (Ploner et al, 1998; White et al, 1994; Wimmer et al, 2014). More important for multi-item WM tasks is the impact of item number on the reliability of storage (Ma et al, 2014). Here, we have shown that interactions in item memory can be described by the dynamics of multiple bumps in a common networks. Specifically, items that are closer to one another will lead to stronger interactions in the bumps that they instantiate, leading to bump annihilations or repulsions. Notably, our mechanism is much more suggestive of the resource model of WM (Bays and Husain, 2008) than of a slots model, which would assume that the first few items stored do not have associated memories that interact in any way (Zhang and Luck, 2008).

5 Discussion

Working memory is a central feature of cognition, which plays an important role in attention (Gazzaley and Nobre, 2012) and motor planning (Ikkai and Curtis, 2011). Limitations on the fidelity of working memory can therefore limit other cognitive functions. We have proposed a simplified model to account for item and temporal limitations in multi-item WM, based on recent studies of spiking networks (Almeida et al, 2015; Wei et al, 2012). Similar to these previous studies, we associate the memory of an item in space with the location of a bump attractor, subject to fluctuations and interactions with other bumps.

The advantage of our model is that we were able to analyze the dynamics of the network, and reduce the dynamics to a low-dimensional system describing the interfaces of the bumps. Errors in recall occur due to merging, repulsion, and annihilation events resulting from bump interactions, which can also be captured by the corresponding interface equations. This is in addition to the typical fluctuation-induced errors known to arise during the delay period of visual WM tasks (Constantinidis and Klingberg, 2016; Wimmer et al,

2014). Importantly, we have show that the strength of synaptic coupling in a recurrent network shapes the mean squared error (MSE) in WM tasks. More weakly coupled networks support narrower bump attractors that interact less, but are more subject to noise fluctuations. Strongly coupled networks possess wider bumps, which are less subject to noise fluctuations. There is an optimal scaling of synaptic strength that minimizes the MSE, trading off reduced effects of noise with bumps that are not too wide. This optimal scaling strength decreases for tasks requiring memory of more items.

Interface methods were used to reduce the neural field model to a system of a few differential equations, corresponding to the threshold crossing points of dynamically evolving bumps. An exact description of the evolution of the interfaces can be obtained by evolving an integral equation describing the dynamically evolving gradient at the interfaces (Coombes et al, 2012). However, these integral equations are much less straightforward to derive in the case when stochastic forcing is incorporated into the evolution equations, so we employed a static gradient approximation, ignoring the perturbations of the gradient near the interfaces. We expect that interface equations that capture these fluctuations in the gradient would provide a more accurate approximation of the dynamics of the full neural field model, Eq. (2.1). Nonetheless, we were able to derive a reasonably accurate approximation for the dynamics of multiple remembered items during the delay period of a WM task.

Controversy still remains as to whether errors in multiple item WM are best explained using a slots (Zhang and Luck, 2008) or resource (Bays and Husain, 2008) model of item storage. Our model mostly supports the latter hypothesis, since recall errors depend on the item number across all item counts. Furthermore, we expect that the practical capacity of the network will be relatively high, since many bumps can be stored in a single recurrent network, and there will not tend to be an abrupt drop in accuracy at any particular item count. Thus, we see no strong evidence of a small and fixed capacity in our model. Rather, the capacity of the network is much larger, and would likely not be revealed by the typical item counts used in WM experiments (Ma et al, 2014). Furthermore, our model predicts that if two angles are initially placed close to one, there will be more error in recalling their locations. This is due to the nonlinear interactions in the network. This is consistent with a recent experimental study of multi-item working memory tasks analyzed in Almeida et al (2015).

We could also extend our model to consider WM for objects residing in a higher-dimensional feature space, such as two-dimensional position or the combination of both color and position. Note that some working memory tasks implicitly require subjects to remember both the color and position of remembered items, so that, for example, the color can be used to indicate which item the subject should recall (Bays and Husain, 2008). Thus, it may be more realistic to consider the dynamics of stored variables interacting on two-dimensional domains, and this would also aid in providing a mechanistic explanation for swap errors. Swap errors can occur when a subject uses the stored location of a different item to report the remembered location of a cued item (Bays et al, 2009). Thus, it may be that both item interactions and fluctuations that produce errors in the stored position may affect the stored color in a similar way.

Our mechanistic model of multiple item WM limitations has a distinct advantage over heuristic parameterized models, in that it is linked to constraints of physiology. However, we expect there are many extensions of the framework, which would likely more reliably reflect actual physiology. In particular, while there is evidence for persistent neural activity in visual WM, we expect that the strongly bistable nature of bumps in Eq. (2.1) may be inconsistent with the various accumulating and decaying activity traces observed in some cortical during WM tasks (Murray et al, 2016; Zylberberg and Strowbridge, 2017). Such temporally heterogeneous activity, distinct from the relatively stable trace a bump attractor, may still provide a stable population code. Thus, it would be interesting to explore how dynamic neural activity traces representing different item would interact in a computational model, and whether the principles of a resource-type model of WM would arise there as well.

Acknowledgements

NK was supported by EXTREEMS - QED: Directions in Data Discovery in Undergraduate Education (NSF DMS-1407340). ZPK was supported by an NSF grant (DMS-1615737).

References

Almeida R, Barbosa J, Compte A (2015) Neural circuit basis of visuo-spatial working memory precision: a computational and behavioral study. *Journal of neurophysiology* 114(3):1806–1818

- Amari S (1977) Dynamics of pattern formation in lateral-inhibition type neural fields. *Biol Cybern* 27(2):77–87
- Amari Si (2014) Heaviside world: Excitation and self-organization of neural fields. In: *Neural Fields*, Springer, pp 97–118
- Barak O, Tsodyks M (2014) Working models of working memory. *Current opinion in neurobiology* 25:20–24
- Bays PM (2015) Spikes not slots: noise in neural populations limits working memory. *Trends in cognitive sciences* 19(8):431–438
- Bays PM, Husain M (2008) Dynamic shifts of limited working memory resources in human vision. *Science* 321(5890):851–854
- Bays PM, Catalao RF, Husain M (2009) The precision of visual working memory is set by allocation of a shared resource. *Journal of vision* 9(10):7–7
- Van den Berg R, Shin H, Chou WC, George R, Ma WJ (2012) Variability in encoding precision accounts for visual short-term memory limitations. *Proceedings of the National Academy of Sciences* 109(22):8780–8785
- Bressloff PC (2005) Weakly interacting pulses in synaptically coupled neural media. *SIAM Journal on Applied Mathematics* 66(1):57–81
- Bressloff PC (2009) Stochastic neural field theory and the system-size expansion. *SIAM Journal on Applied Mathematics* 70(5):1488–1521
- Bressloff PC (2012) Spatiotemporal dynamics of continuum neural fields. *Journal of Physics A: Mathematical and Theoretical* 45(3):33,001–33,109
- Bressloff PC, Webber MA (2012) Front propagation in stochastic neural fields. *SIAM Journal on Applied Dynamical Systems* 11(2):708–740
- Buschman TJ, Siegel M, Roy JE, Miller EK (2011) Neural substrates of cognitive capacity limitations. *Proceedings of the National Academy of Sciences* 108(27):11,252–11,255
- Carroll S, Josić K, Kilpatrick Z (2014) Encoding certainty in bump attractors. *Journal of computational neuroscience* 37(1):29–48
- Compte A, Brunel N, Goldman-Rakic PS, Wang XJ (2000) Synaptic mechanisms and network dynamics underlying spatial working memory in a cortical network model. *Cerebral Cortex* 10(9):910–923
- Constantinidis C, Klingberg T (2016) The neuroscience of working memory capacity and training. *Nature Reviews Neuroscience* 17(7):438–449
- Coombes S, Laing C (2011) Pulsating fronts in periodically modulated neural field models. *Physical Review E* 83(1):011,912
- Coombes S, Owen MR (2005) Bumps, breathers, and waves in a neural network with spike frequency adaptation. *Physical Review Letters* 94(14):148,102
- Coombes S, Schmidt H (2010) Neural fields with sigmoidal firing rates: approximate solutions. *Discrete and Continuous Dynamical Systems Series S*
- Coombes S, Schmidt H, Bojak I (2012) Interface dynamics in planar neural field models. *The Journal of Mathematical Neuroscience* 2(1):9
- Cowan N (2010) The magical mystery four: How is working memory capacity limited, and why? *Current directions in psychological science* 19(1):51–57
- Ermentrout B (1998) Neural networks as spatio-temporal pattern-forming systems. *Reports on progress in physics* 61(4):353
- Fougnie D, Suchow JW, Alvarez GA (2012) Variability in the quality of visual working memory. *Nature communications* 3:1229
- Funahashi S, Bruce CJ, Goldman-Rakic PS (1989) Mnemonic coding of visual space in the monkey9s dorsolateral prefrontal cortex. *Journal of neurophysiology* 61(2):331–349
- Gardiner C (2009) *Handbook of stochastic methods*, 4th edition. Springer
- Gazzaley A, Nobre AC (2012) Top-down modulation: bridging selective attention and working memory. *Trends in cognitive sciences* 16(2):129–135
- Gökçe A, Avitabile D, Coombes S (2017) The dynamics of neural fields on bounded domains: an interface approach for dirichlet boundary conditions. *Journal of Mathematical Neuroscience*
- Goldman-Rakic PS (1995) Cellular basis of working memory. *Neuron* 14(3):477–485
- Gorgoraptis N, Catalao RF, Bays PM, Husain M (2011) Dynamic updating of working memory resources for visual objects. *Journal of Neuroscience* 31(23):8502–8511
- Guo Y, Chow CC (2005) Existence and stability of standing pulses in neural networks: Ii. stability. *SIAM Journal on Applied Dynamical Systems* 4(2):249–281
- Ikkai A, Curtis CE (2011) Common neural mechanisms supporting spatial working memory, attention and motor intention. *Neuropsychologia* 49(6):1428–1434

- Keshvari S, Van den Berg R, Ma WJ (2013) No evidence for an item limit in change detection. *PLoS computational biology* 9(2):e1002927
- Kilpatrick ZP (2013) Interareal coupling reduces encoding variability in multi-area models of spatial working memory. *Frontiers in computational neuroscience* 7
- Kilpatrick ZP (2016) Ghosts of bump attractors in stochastic neural fields: Bottlenecks and extinction. *Discrete Contin Dyn Syst Ser B* 21:2211–2231
- Kilpatrick ZP (2017) Synaptic mechanisms of interference in working memory. *bioRxiv* p 149435
- Kilpatrick ZP, Ermentrout B (2013) Wandering bumps in stochastic neural fields. *SIAM Journal on Applied Dynamical Systems* 12(1):61–94
- Kilpatrick ZP, Ermentrout B, Doiron B (2013) Optimizing working memory with heterogeneity of recurrent cortical excitation. *The Journal of Neuroscience* 33(48):18,999–19,011, DOI 10.1523/JNEUROSCI.1641-13.2013, URL <http://www.jneurosci.org/content/33/48/18999.abstract>, <http://www.jneurosci.org/content/33/48/18999.full.pdf+html>
- Laing CR, Troy WC (2003a) Pde methods for nonlocal models. *SIAM Journal on Applied Dynamical Systems* 2(3):487–516
- Laing CR, Troy WC (2003b) Two-bump solutions of amari-type models of neuronal pattern formation. *Physica D: Nonlinear Phenomena* 178(3):190–218
- Laing CR, Troy WC, Gutkin B, Ermentrout GB (2002) Multiple bumps in a neuronal model of working memory. *SIAM Journal on Applied Mathematics* 63(1):62–97
- Lara AH, Wallis JD (2012) Capacity and precision in an animal model of visual short-term memory. *Journal of Vision* 12(3):13–13
- Lu Y, Sato Y, Amari Si (2011) Traveling bumps and their collisions in a two-dimensional neural field. *Neural Computation* 23(5):1248–1260
- Luck SJ, Vogel EK (1997) The capacity of visual working memory for features and conjunctions. *Nature* 390(6657):279
- Luck SJ, Vogel EK (2013) Visual working memory capacity: from psychophysics and neurobiology to individual differences. *Trends in cognitive sciences* 17(8):391–400
- Ma WJ, Husain M, Bays PM (2014) Changing concepts of working memory. *Nature neuroscience* 17(3):347–356
- Murray JD, Bernacchia A, Roy NA, Constantinidis C, Romo R, Wang XJ (2016) Stable population coding for working memory coexists with heterogeneous neural dynamics in prefrontal cortex. *Proceedings of the National Academy of Sciences* p 201619449
- Novikov EA (1965) Functionals and the random-force method in turbulence theory. *Sov Phys JETP* 20(5):1290–1294
- Pinto DJ, Ermentrout GB (2001) Spatially structured activity in synaptically coupled neuronal networks: I. lateral inhibition and standing pulses. *SIAM Journal on Applied Mathematics* 62(1):226–243
- Ploner CJ, Gaymard B, Rivaud S, Agid Y, Pierrot-Deseilligny C (1998) Temporal limits of spatial working memory in humans. *European Journal of Neuroscience* 10(2):794–797
- Wei Z, Wang XJ, Wang DH (2012) From distributed resources to limited slots in multiple-item working memory: a spiking network model with normalization. *Journal of Neuroscience* 32(33):11,228–11,240
- White JM, Sparks DL, Stanford TR (1994) Saccades to remembered target locations: an analysis of systematic and variable errors. *Vision research* 34(1):79–92
- Wilken P, Ma WJ (2004) A detection theory account of change detection. *Journal of vision* 4(12):11–11
- Wimmer K, Nykamp DQ, Constantinidis C, Compte A (2014) Bump attractor dynamics in prefrontal cortex explains behavioral precision in spatial working memory. *Nature neuroscience* 17(3):431–439
- Zhang W, Luck SJ (2008) Discrete fixed-resolution representations in visual working memory. *Nature* 453(7192):233
- Zylberberg J, Strowbridge BW (2017) Mechanisms of persistent activity in cortical circuits: possible neural substrates for working memory. *Annual Review of Neuroscience* 40